



Full Text View

[Volume 29, Issue 6 \(June 1999\)](#)

Journal of Physical Oceanography

Article: pp. 1221–1238 | [Abstract](#) | [PDF \(254K\)](#)

A Turbulent Bottom Boundary Layer Code for Use in Numerical Ocean Models

Peter D. Killworth and Neil R. Edwards

Southampton Oceanography Centre, Southampton, United Kingdom

(Manuscript received July 23, 1997, in final form June 23, 1998)

DOI: 10.1175/1520-0485(1999)029<1221:ATBBLC>2.0.CO;2

ABSTRACT

A model for a turbulent bottom boundary “slab” layer is described. The model is designed to fit under a standard, depth coordinate ocean general circulation model, with a view to improving its response both for local and climate problems. The depth of the layer varies temporally and spatially. Both analytical and numerical versions of the model conserve energy. The model is tested using a source of dense water on a slope, and performs satisfactorily, with the plume spreading far more than the equivalent case without a bottom layer.

1. Introduction

It has long been known (cf. [Armi and Millard 1976](#)) that there is a turbulent layer near the bottom, of thickness 10–50 m, whose temperature and salinity are well mixed in the vertical: the bottom equivalent of a surface mixed layer, in fact. The behavior of water within these layers is of vital importance to the global thermohaline circulation because outflows from areas of deep-water formation, which pass over sills between basins, descend to the ocean floor as bottom boundary layers. Typical are the outflows from the Mediterranean, through the Denmark and Iceland–Faeroes Straits, areas of dense water around the Antarctic, the deep western boundary countercurrents, etc., although dense bottom layers are *ubiquitous* in the ocean ([Pratt and Lundberg 1991](#) give a survey of sill flows).

However, we still know very little about bottom boundary layers, save in well-surveyed regions such as the Mediterranean outflow ([Johnson et al. 1994](#)). There is clear evidence of turbulent mixing within the layers, but under what circumstances there is entrainment or detrainment is far from clear. The mixed layer at the ocean surface normally entrains when there is surface cooling and detrains when there is sufficient surface heating, but there is no corresponding interfacial heat flux for the bottom mixed layer. Whether the layer entrains or detrains depends on the balance between two sources of turbulent energy—bottom friction and internal waves, plus possible external sources (e.g., tidal mixing)—and two sinks—turbulent dissipation, which is normally modeled as a fraction of the energy inputs and so is never large enough to counter the sign of the inputs, and entrainment itself.

Lack of a bottom boundary layer model in level general circulation models has an immediate impact on the water mass structure in those models (C. Gordon 1996, personal communication). In such models, dense water passing over a sill finds itself one grid point above less dense water beneath it. The resulting convective overturn, usually repeated downstream over several grid points, results in the dense water mass becoming heavily diluted from its original value, thus destroying the

Table of Contents:

- [Introduction](#)
- [The bottom boundary layer](#)
- [Numerical implementation](#)
- [A test problem](#)
- [Discussion](#)
- [REFERENCES](#)
- [APPENDIX](#)
- [FIGURES](#)

Options:

- [Create Reference](#)
- [Email this Article](#)
- [Add to MyArchive](#)
- [Search AMS Glossary](#)

Search CrossRef for:

- [Articles Citing This Article](#)

Search Google Scholar for:

- [Peter D. Killworth](#)
- [Neil R. Edwards](#)


water mass structure in the recipient basin.⁴

Semianalytical models of the bottom boundary layer in regions of outflow have existed for over 20 years ([Smith 1975](#); [Killworth 1977](#); [Price and Baringer 1994](#)). These traditionally use a streamtube. In this approach, the outflow is assumed to occur in a confined tube whose velocity, temperature, and salinity are assumed constant over a cross section normal to the mean flow. Predictive equations are produced to give the downstream variation of properties and include turbulent friction, entrainment, and other features. These models can be tuned to give a good fit to observations (e.g., [Price and Baringer 1994](#)) if certain ad hoc assumptions about the aspect ratio of the streamtube are made. However, recent work ([Emms 1998a](#)) suggests that apparently trivial changes to the physics of the model can induce dramatic changes in its behavior, so the agreement may be fortuitous.

[Jungclaus and Backhaus \(1994\)](#) extended the model from one to two dimensional. Apart from numerical difficulties near the edge of the layer, the model system was able to reproduce observed features well and in one case ([Jungclaus et al. 1995](#)) demonstrated a splitting of a streamtube into two at a saddle point in topography in a realistic manner. Recently, the effects of suspended particulate matter, which have a very strong effect on density, have been included in two-dimensional ([Fohrmann et al. 1998](#)) and streamtube models ([Emms 1998b](#)).

The above models all possess two shortcomings. First, the codes are divorced from large-scale general circulation models because they are still quasi analytical (i.e., numerical approaches are used to solve the problem). Second, all of the models mentioned permit turbulent *entrainment*, which can be cut off under certain stability conditions, but none permit *detrainment* of water from the bottom boundary layer. Integration of such models under an ocean general circulation model would result in a gradual removal of water from the ocean interior, by entrainment, into the bottom boundary layer so that eventually the entire ocean would be subsumed into the bottom layer.

Three extant numerical models explicitly include a bottom boundary layer. First, the Sandia model ([Dietrich et al. 1987](#)) has a multilayer turbulent bottom boundary layer in terrain-following coordinates added to a slab representation of the lowest grid point. This scheme has obvious advantages: the bottom layer is explicitly calculated so that the parameterization of its physics is minimized. Also, the [Mellor–Yamada \(1974\)](#) closure scheme used in the [Dietrich et al. \(1987\)](#) model formally permits an increase of turbulence near the floor if the physics requires it. Such an approach is attractive and covers both surface and floor boundary layers equally well, but at the cost of additional complexity in the equations for turbulent energy, etc., which are required. However, the ocean interior above the layer is still described by a single gridpoint value so that one is grafting on a system with many degrees of freedom to an interior point with precisely one degree of freedom. Second, [Beckmann and Döscher \(1997\)](#) couple a terrain-following bottom boundary layer to a interior level coordinate system, but choose a simplification whereby only tracer tendencies are evaluated in the terrain-following coordinate system with velocities, etc., taken from the near-bottom interior values. Third, [Gnanadesikan \(1999\)](#) takes the [Beckmann and Döscher \(1997\)](#) approach one stage further by using the analytically correct pressure gradient within the bottom boundary layer and permitting direct flow between the bottom layers. However, the layer thickness is prespecified so that turbulence is modeled with a turbulence coefficient rather than with entrainment/detrainment.

The approach taken in this paper is intermediate between the full boundary layer approach and a simple parameterization. The idea is to pose consistent equations for a “slab” boundary layer that occupies some time- and spatially varying depth at the ocean floor. These are posed in a continuous model, which permits straightforward tests of consistency if required. The equations are then cast into finite-difference form. In most level models, the ocean floor has a stepped topography, with a locally flat bottom below tracer (temperature, salinity, etc.) points and abrupt changes at the box edge. The boundary layer now occupies a (locally flat) fraction of the bottom tracer box. At the edge of the box, outflow from the boundary layer rises or falls instantaneously to the side of the next box laterally, as indicated schematically in [Fig. 1](#) . Outflow from the remainder of the bottom grid box flows purely horizontally (although through an area whose size will depend on the thickness of the bottom boundary layer).

[Section 2](#) discusses the continuous formulation, and [section 3](#) the numerical implementation into a free surface model (MOMA; [Webb 1996](#)). [Section 4](#) gives an example, and [section 5](#) discusses the model.

2. The bottom boundary layer model

The continuous form of the equations is given here, although some aspects of the finite-difference version must inevitably intrude because of the manner in which we have chosen to handle turbulent entrainment (ignoring convection for clarity).

In the ocean interior, standard Boussinesq Navier–Stokes equations are assumed to apply:

$$p_z = -g\rho \quad (2.3)$$

$$u_x + v_y + w_z = 0 \quad (2.4)$$

$$T_t + \mathbf{u} \cdot \nabla T = K_H(T_{xx} + T_{yy}) + K_V T_{zz} \quad (2.5)$$

$$S_t + \mathbf{u} \cdot \nabla S = K_H(S_{xx} + S_{yy}) + K_V S_{zz} \quad (2.6)$$

$$\rho = \rho(T, S, z). \quad (2.7)$$

These are, respectively, conservation of east and north momentum, the hydrostatic relation, zero flow divergence, conservation of heat and salt, and the equation of state; standard notation is used. Turbulent coefficients for momentum and tracers have been assumed, but other forms can be used. (The code below uses spherical polar coordinates, but these are omitted here for clarity.)

These equations hold in the interior of the fluid, between the surface $z = 0$ (numerically the surface is taken as a free surface, though a rigid lid can equally well be used) and a height $h(x, y, t)$ above the bottom $z = -D(x, y)$; here $h(x, y, t)$ represents the thickness of the bottom boundary layer. Rather than the normal bottom boundary conditions, vertical turbulent fluxes vanish at $z = -D + h$; they are replaced by the effects of entrainment/detrainment.

We now proceed to develop equations for the slab bottom layer. For clarity of exposition we will initially assume that all required quantities such as layer height and entrainment velocity can be expressed as continuous differentiable functions of time. For reasons given below, we will subsequently modify this approach.

Assume that the boundary layer is locally entraining with entrainment velocity w^* . Then by continuity, w^* satisfies

$$\begin{aligned} w^* &= h_t - w_i - \mathbf{u}_i \cdot \nabla(D - h) \\ &= h_t + \nabla \cdot (h\mathbf{u}_m), \end{aligned} \quad (2.8)$$

where subscripts i and m denote interior and boundary values respectively (interior values are here taken just above the boundary layer, and boundary layer values are assumed independent of height). The situation is modified when the layer is detraining. Equations for slab conservation of tracers and momentum are then

$$\begin{aligned} (hu_m)_t + \nabla \cdot (h\mathbf{u}_m u_m) - w^* u_i - fhv_m \\ = -h \frac{\overline{p_{mx}}}{\rho_0} + A_H \nabla \cdot (h \nabla u_m) - C_D |\mathbf{u}_m| u_m \end{aligned} \quad (2.9)$$

$$\begin{aligned} (hv_m)_t + \nabla \cdot (h\mathbf{u}_m v_m) - w^* v_i + fhu_m \\ = -h \frac{\overline{p_{my}}}{\rho_0} + A_H \nabla \cdot (h \nabla v_m) - C_D |\mathbf{u}_m| v_m \end{aligned} \quad (2.10)$$

$$(hT_m) - w^* T_i + \nabla \cdot (h\mathbf{u}_m T_m) = K_H \nabla \cdot (h \nabla T_m) \quad (2.11)$$

$$(hS_m) - w^* S_i + \nabla \cdot (h\mathbf{u}_m S_m) = K_H \nabla \cdot (h \nabla S_m), \quad (2.12)$$

where there is a quadratic bottom stress with coefficient C_D . It is perfectly straightforward to add other dissipative terms (cf. [Gnanadesikan 1999](#)) to represent external and other energy sinks, for example, tidal mixing. The divergence and gradient operators are here two-dimensional. If the layer is detraining, interior values are replaced by boundary layer values in the w^* terms. Similar terms occur as boundary conditions for the interior quantities.

The ‘‘pressure gradients’’ in (2.9), (2.10) are not true gradients, but instead are depth-averaged pressure gradients over the layer. Some care is needed with these terms to minimize any erroneous pressure gradients produced in a similar manner to those that occur when sigma coordinates are used ([Haney 1991](#)). To obtain the expressions, let $z = -H$ be some level surface in the fluid interior. Then within the bottom layer,

$$p = p_{-H} - g \int_{-H}^{-D+h} \rho_l dz - g(z + D - h)\rho_m, \quad (2.13)$$

where a subscript I denotes interior values (which vary with depth). The first two terms are the pressure at the top of the boundary layer, p_i . Then

$$\begin{aligned}\overline{\nabla p_m} &\equiv \frac{1}{h} \int_{-D}^{-D+h} \nabla p \, dz \\ &= \nabla \left(p_{-H} - g \int_{-H}^{-D+h} \rho_I \, dz \right) - g \rho_m \nabla(D - h) \\ &\quad + \frac{gh}{2} \nabla \rho_m \\ &= \nabla p_i - g \rho_m \nabla(D - h) + \frac{gh}{2} \nabla \rho_m \quad (2.14)\end{aligned}$$

$$= \nabla p_m - g \rho_m \nabla \left(D - \frac{h}{2} \right), \quad (2.14a)$$

where p_m is the pressure at the center of the bottom boundary layer. This latter expression—used in the actual code—is identical to [Gnanadesikan's \(1999\)](#) formulation with the exception of the last term (he assumes h to be very small in this context). He gives three cases in which no error in pressure gradient occurs: uniform interior density and a different (uniform) bottom layer density, a uniform interior, and density a linear function of depth. It follows that for vanishingly small h the same holds here. (However, there must be a pressure gradient for uniform linear stratification when h is not small since any chosen value for density in the bottom boundary layer will cause a pressure gradient to occur if h varies.) In the discretized form of these test problems, pressure gradient errors occur anyway. For these and for more general density distributions, the size of the error is generally small except for steep slopes or when a step in topography occupies many grid points, which [Hughes \(1995\)](#) has argued should be avoided on energy grounds. Appendix B discusses pressure gradient errors.

In order for [\(2.14\)](#) to reduce to known results when applied numerically, it is necessary to modify the way that the hydrostatic relation is computed between the lowest interior grid box and the bottom boundary layer. For energy conservation, normal MOM-like codes evaluate $p_k - p_{k-1}$ as $(g/4)(\Delta z_{k-1} + \Delta z_k)(\rho_{k-1} + \rho_k)$ (cf. [Cox 1984](#)) between levels $k - 1$ and k . It is important to revise this near the bottom by explicitly integrating with the in situ density values, so $p_m - p_I$ is evaluated as $g(\Delta z/2 - h)\rho_I + gh\rho_m/2$.

Then, it is easily seen that [\(2.14\)](#) reduces to known values in various limits. For example, if p_{-H} and ρ_I are both constant, then $\overline{\nabla p_m}$ vanishes if D , h , and ρ_m are all constant. If only ρ_m is allowed to vary, [\(2.14\)](#) gives $\overline{\nabla p_m} = (gh/2)\nabla \rho_m$ as in [Jungclaus and Backhaus \(1994\)](#); this is not the case using the original Cox formulation. If instead h is allowed to vary, $\overline{\nabla p_m} = g(\rho_m - \rho_I)\nabla h$, again as in [Jungclaus and Backhaus \(1994\)](#); this is again not the case using the Cox approach. Finally, if D , h , and ρ_m all vary,

$$\overline{\nabla p_m} = -g(\rho_m - \rho_I)\nabla(D - h) + \frac{gh}{2}\nabla \rho_m,$$

as used by [Jungclaus and Backhaus \(1994\)](#). Note that this would be represented solely as $-g(\rho_m - \rho_I)\nabla D$ (probably the dominant term under most circumstances) in [Gnanadesikan's \(1999\)](#) simplified formulation.

It will appear in the discrete version that the pressure gradient is also modified in the lowest interior layer; this will be discussed in [section 3](#).

These equations are to be completed with a specification of w^* , which in the case of a surface mixed layer would be derived from a turbulent energy equation for the rate of change of layer thickness. However, as noted above, it is difficult to formulate a simple energy equation that permits detrainment, in contrast to the case of a surface mixed layer, without some ad hoc way to specify energy dissipation. Accordingly, this approach is inconvenient in a model. Another practical reason caused the abandonment of this approach. Numerical tests showed, and simple analysis confirmed, that a plus-minus temporal behavior built up rapidly when simple functional forms for w^* were taken, with boundary layer thicknesses oscillating between two unphysical values.

A second method was adopted here. The approach is similar to that used for many implementations of surface boundary layers. Equations for slab conservation of tracers and momentum are made for the bottom layer as before, together with conservation of layer thickness, where now entrainment or detrainment is *neglected*; that is, the w^* terms in (2.8) to (2.12) are neglected. In other words, the layer acts as if there is a thin membrane between it and the interior fluid. The effects of turbulence are then added a posteriori, in this case at the end of each time step when a suitable formula for layer thickness based on momentum and tracers in the interior and the layer is applied (Zilitinkevich and Mironov 1996).² The resulting adjustment in bottom boundary height is considered to represent the effects of entrainment if the layer has deepened, or detrainment if the layer has become thinner. Tracers and momentum are simply removed from the interior (boundary layer) and mixed into the boundary layer (interior) depending as the layer is entraining (detraining).

Then the equations satisfied by the bottom layer are exactly (2.8) to (2.12) without the w^* terms; that is,

$$h_t + \nabla \cdot (h\mathbf{u}_m) = 0 \quad (2.15)$$

$$\begin{aligned} (h\mathbf{u}_m)_t + \nabla \cdot (h\mathbf{u}_m\mathbf{u}_m) - fh\mathbf{v}_m \\ = -h\frac{\overline{p_{mx}}}{\rho_0} + A_H\nabla \cdot (h\nabla\mathbf{u}_m) - C_D|\mathbf{u}_m|\mathbf{u}_m \end{aligned} \quad (2.16)$$

$$\begin{aligned} (h\mathbf{v}_m)_t + \nabla \cdot (h\mathbf{u}_m\mathbf{v}_m) + fh\mathbf{u}_m \\ = -h\frac{\overline{p_{my}}}{\rho_0} + A_H\nabla \cdot (h\nabla\mathbf{v}_m) - C_D|\mathbf{u}_m|\mathbf{v}_m \end{aligned} \quad (2.17)$$

$$(hT_m)_t + \nabla \cdot (h\mathbf{u}_mT_m) = K_H\nabla \cdot (h\nabla T_m) \quad (2.18)$$

$$(hS_m)_t + \nabla \cdot (h\mathbf{u}_mS_m) = K_H\nabla \cdot (h\nabla S_m). \quad (2.19)$$

Essentially this is a form of equilibrium turbulence closure for the bottom boundary layer. We assume that the layer is always in a local equilibrium state in which its depth depends on local mean gradients in the vertical. A necessary condition for this to be justified is that a timescale for the layer to return to one-dimensional equilibrium is small compared with a timescale for changes in the mean flow. It would be straightforward to modify this approach to a relaxation toward an equilibrium depth given an estimate of an appropriate relaxation timescale.

While this approximation may be too crude for some problems, it is particularly appropriate for a general extension to MOM-like codes, as it is closely analogous to the turbulence closure in the interior of the fluid, which is of the eddy viscosity, or lowest order closure. In such a closure, the level of turbulence depends only on spatially and temporally local values of mean gradients.

There is a wide literature on turbulent mixed layers; Nurser (1996) gives a thorough review. Little work exists on bottom boundary layers themselves (Armi and Millard 1976) save for overflow regions and other specialized areas such as the HEBBLE experiment. Even in these well documented regions, estimating entrainment is not easy (cf. Baringer and Price 1997b). Zilitinkevich and Mironov (1996) have proposed an expression for the equilibrium depth of a turbulent, stably stratified boundary layer including the effects of rotation, buoyancy flux, and static stability. Their work is aimed mainly at boundary layers whose velocity field exceeds that in the interior, so the appropriate Richardson number is one based on the bottom layer velocity. Armi and Millard (1976) find a best fit to data using such a number. An alternative Richardson number based on velocity jumps across the layer interface is frequently used in modeling of streamtubes (e.g., Price and Baringer 1994) since it governs the production of internal wave energy through instability. In the case of a quiescent interior, the two Richardson numbers are of course identical.

In the case of a bottom boundary layer where there is no buoyancy flux, Zilitinkevich and Mironov's three-term formulation reduces to

$$\left(\frac{h}{C_n u_* / f}\right)^2 + \frac{h}{C_i u_* / N} = 1, \quad (2.20)$$

where C_n , C_i are constants; u_* is the surface friction velocity—here taken as given by $u_*^2 = C_D|\mathbf{u}_m|^2$ —and N is the background buoyancy frequency. This provides a smooth transition for the depth h between a value dominated by the Rossby and Montgomery (1935) value $C_n u_* / f$, when the stratification is weak, to a value dominated by Deardorff's (1972) indicated value $C_i u_* / N$, when stratification is strong or rotation weak, for example, near the equator. Zilitinkevich and Mironov (1996) suggest $C_n = 0.5$, $C_i = 20$.³

Numerically, the quantity N is awkward to compute since, as a gradient, it formally involves tracer values one and two grid points above the bottom. It is not obvious that density gradients far from the bottom boundary layer are relevant to the layer dynamics. Instead, we choose to use a value estimated by

$$N^2 = \frac{g(\Delta\rho/\rho_0)}{h} \equiv \frac{g'}{h}, \quad (2.21)$$

where $\Delta\rho = \rho_m - \rho_l$ and the distance over which the density gradient is taken is the width of the boundary layer (a simple estimate based on grid spacing would yield answers varying with resolution; it seems simpler to assume that the gradient is felt over a distance whose order is the mixed layer depth). [Armi and Millard \(1976\)](#) use the same approach, though with slightly different emphasis: they assume the bottom layer to be produced by purely local vertical mixing so that its density can be directly calculated from the layer depth and interior stratification. Applying the formula $h = C_l u_*^*/N$ then leads to

$$h = \frac{C_i^2 u_*^2}{g'} = C_i^2 C_D \frac{|\mathbf{u}_m|^2}{g'}. \quad (2.22)$$

Using $C_D = 0.003$ gives the coefficient in [\(2.22\)](#) as 1.2.

Thus we rewrite [\(2.20\)](#) slightly as

$$\left(\frac{h}{C_n u_*^*/f} \right)^2 + \frac{h}{C_k |\mathbf{u}_m|^2 / g'} = 1, \quad (2.23)$$

where $C_k = C_i^2 C_D$, which is used henceforth. It is straightforward to replace [\(2.23\)](#) by a different formula in the code if desired. [Figure 2](#) shows contours of h from [\(2.23\)](#) using the default values, at 30° latitude. For large density contrasts, [\(2.23\)](#) is dominated by the second term on the lhs, while, for smaller density contrasts, the Coriolis term dominates; the smooth transition between the two is clearly demonstrated by [Fig. 2](#). Note that layer depth is a fairly sensitive function of the parameters, none of which is well defined from observations.

When $u_*^*/N \ll u_*^*/f$, the second term in [\(2.23\)](#) dominates, in which case [\(2.23\)](#) is equivalent to specifying the bulk Froude number

$$\text{Fr} = \frac{|\mathbf{u}_m|}{(g'h)^{1/2}}$$

of the layer to be a constant ($1/C_k^{1/2}$). For the values given above, this is 0.9, though this value is obviously sensitive to parameter variation. Observations in turbulent outflow plumes such as the Mediterranean outflow ([Baringer and Price 1997a](#)) show Froude numbers varying from 0.1 to over unity. Here, it is clear, a local vertical equilibrium parameterization is not a complete solution to the entrainment–detrainment problem that we seek to solve; but it is a first step toward a more complete solution.

In a slope configuration for a streamtube model, the alongslope velocity u_m is usually given by the geostrophic relation $u_m = g'\alpha/f$, where α is the topographic slope ([Killworth 1977](#); [Price and Baringer 1994](#)). Combining this with the Froude number relationship defines the depth $h = C_k g'\alpha^2/f^2$ as a function of the environmental parameters. In particular, h varies as g' , so denser plumes (relative to their environment) are thicker. Thus the thickness of a downslope plume is limited by this method, which in turn means that—other things being equal—for a plume with this formulation to carry more flux, it must become wider rather than thicker.

We now imagine the situation after a time step in which h has been predicted by [\(2.15\)](#). The boundary layer depth has thus changed because of large-scale divergence or convergence of the flux in the layer. In addition, turbulent effects must be included. The modified [Zilitinkevich and Mironov \(1996\)](#) formula [\(2.23\)](#) is applied at each point to give a value h_{new} , or equivalently a change $\Delta h = h_{\text{new}} - h$ between the formula value and that obtained from the large-scale dynamics. If Δh is positive, the layer is entraining; if negative, the layer is detraining.

In the *entraining* case, interior values are left unaltered (although part of the interior is swallowed by the now thicker boundary layer), but boundary layer values are now modified,

$$T_{m,\text{new}} = \frac{1}{h_{\text{new}}}(hT_m + \Delta hT_l) \quad (\text{entraining}), \quad (2.24)$$

with similar treatment for other variables. There is an implicit assumption in (2.24) that interior values do not change over the vertical distance Δh . Alternatively, (2.24) can be thought of as an equation connecting $\partial T_m / \partial t$ with $\partial h / \partial t$. In the detraining case, boundary layer values are left unaltered, and interior values are modified above the layer. In a fully continuous case, boundary layer values would simply be left behind as the layer retreated. In the finite-difference case, if the bottom grid spacing is Δz , say, over which the bottom interior value is spread, then

$$T_{I, \text{new}} = \frac{1}{\Delta z - h_{\text{new}}} [(\Delta z - h)T_I - \Delta h T_m] \quad (\text{detraining}). \quad (2.25)$$

Such an approach implicitly assumes the interior to be locally well mixed in the vertical. (For a gridpoint model this holds automatically within the bottom grid point.) If this is not the case, then a gradually detraining layer would leave behind fluid in the interior with the same tracer properties as the layer itself, reducing g' to a very small value. Then (2.23) would imply that h became dominated by the rotation term, and detraining would only continue if either the layer flow was convergent or if the flow speed was decreasing (e.g., if there were no interior geostrophic flow).

In regions of weak flow, (2.23) predicts thin boundary layers; the code as written includes a minimum layer thickness since we imagine the turbulence level to have some background value that would prevent the layer thinning too far. Conversely, in regions of rapid flow, for example, in overflow regions, (2.23) predicts layer depths of at least 100 m. Since the numerical concept (Fig. 1) is that the layer occupies a fraction of the bottom gridpoint depth, too fine a vertical resolution would cause difficulties: the bottom layer would naturally occupy more than one grid point in the vertical. At present we see no convenient way to overcome this problem—although it could be coded with some difficulty—and have set a maximum layer depth, which is locally a fixed fraction of the gridpoint thickness⁴; other formulations (e.g., Beckmann and Döscher 1997) suffer from similar potential problems.

3. Numerical implementation

This section discusses how to add the continuous bottom boundary layer model into a B-grid finite-difference model (MOMA: Webb 1996, although any code based on Cox's 1984 work suffices). The normal code stores tracer, density, and pressure at the center of grid cells of (horizontally uniform) thickness Δz_ρ . Horizontal velocity is stored at the corners of this grid in the traditional manner, at the same depths as the other fields. Vertical velocities are computed from the divergence equation and are situated at the top of the grid boxes, above either tracer or velocity dependant upon the equation being used. Centered differences and flux forms are used throughout. The barotropic fields (sea-surface elevation and depth-averaged horizontal velocity) are stepped with smaller steps using a time-splitting approach (cf. Killworth et al. 1991).

The idea is to minimize changes to the model and hence to whichever code is used. To this end, most of the additional fields relevant to the bottom boundary layer have been coded by increasing the vertical dimension of the fields by one and defining the new (bottom) value to be that in the bottom boundary layer, no matter what its actual depth. This means that with small modifications much of the existing code remains functional, even when it applies to the bottom boundary layer. Other coding methods are, of course, possible. However, flux conservation details (see below) mean that some essentially three-dimensional fields need to be computed. At present these are not stored three-dimensionally, thus economizing on possibly valuable storage at the cost of additional cpu time.

Interior values are time-stepped as near to normally as possible. To avoid pressure gradient difficulties, the levels at which pressure is evaluated must remain uniform horizontally. This means that, in addition to the requirement in the previous section, the boundary layer cannot occupy more than 50% of the thickness of the bottom grid point, otherwise the boundary layer would overlap the site for the pressure evaluation. This leads to the structure shown schematically in Fig. 3.

As shown in Fig. 3, the presence of the bottom layer leads to spatial and temporal variation of the heights, and hence the volumes, of certain cells. The bottom tracer cell represents the boundary layer and has height $\Delta z_\rho = h$. The layer above the bottom layer also has variable depth $\Delta z_\rho = \Delta z_0 - h$, where Δz_0 is the height of the cell in the absence of the bottom layer. The height of a velocity cell is taken to be the average of the surrounding tracer cell heights:

$$\Delta z_u = \overline{\Delta z_\rho}^x, \quad (3.1)$$

where the averaging notation means (e.g., in the x direction)

$$\bar{a}^x = [a(x + \Delta x/2) + a(x - \Delta x/2)]/2. \quad (3.2)$$

In the bottom layer the average of adjacent bottom layer values is used, and outside the bottom layer the average is taken over adjacent values at the same vertical level, some of which may be modified by the boundary layer while others are not. Where the bottom is not flat this can lead to a change of the effective depth of a fluid column at a velocity point, defined as the sum of the heights of the velocity cells. The change is unavoidable, produced by the stepped nature of the topography.

The effect can be seen in the column centered on the u_B point in Fig. 3. Here, a portion of the bottom layer has been removed from the depth of the lowest internal u cell, u_B , giving it an effective depth $\Delta z - (0 + h')/2$, where the zero reflects the fact that to the left, the cell is interior and so full depth. (Effects normal to the diagram are ignored for clarity). However, the effective depth of the bottom layer at the u'_B point is $(h + h')/2$ so that the total depth at this point is $h/2$ larger than it is in the original code. This change must be taken into account in summing the contributions from individual momentum equations to the forcing for the barotropic mode. Note that the ocean volume remains constant, but the depth over which nonzero velocity is allowed has increased as a result of allowing direct exchange between bottom layer boxes as in Fig. 1. There is a consequent decrease in the depth over which u is set to zero and no momentum equation is evaluated. In Fig. 3, this occurs in the momentum box immediately below u_B .

The fluxes into computational cells depend on the areas of the cell faces, which now have variable height. From Fig. 3 it is clear that the appropriate height for the flux into a velocity cell is given by the adjacent value of Δz_ρ . Taking into account variation along the cell face, it is seen that the appropriate effective height of the velocity cell face a distance $\Delta x/2$ from the cell center is $\overline{\Delta z}_\rho^y$. Changes in the areas of cell faces are implemented in the code in the form of masks. Thus the mask for advection and diffusion in the x direction takes the value $\overline{\Delta z}_\rho^y$. Fluxes in the y direction are defined analogously.

Tracer cell faces lie at discontinuities in the bottom layer height, so the most appropriate definition of the masking area is not as readily apparent. It turns out to be necessary for energetic consistency to define the masks as follows (for further justification see appendix A). The advective flux of a tracer T in the x direction takes the value $\overline{T}^x u \overline{\Delta z}_u^y \Delta y$, and the advective flux of T in the y direction is $\overline{T}^y v \overline{\Delta z}_u^x \Delta x$. Diffusive fluxes in the x direction are masked by the effective height $\overline{\Delta z}_u^y$ and diffusive fluxes in the y direction are defined analogously. Thus even an apparently interior cell, such as that centered on ρ_C in Fig. 3, possesses modified fluxes. [Note that Hughes (1995) has shown for energetic consistency in a Cox-like code, topography should never rise by more than one grid point per horizontal grid point.]

As noted earlier, there is an additional term to the pressure gradient evaluated in the lowest internal grid point (which is not needed in the continuous version). If H denotes the depth of the top of the lowest internal grid point, then the pressure halfway down the box (at height $-H - D/2$) is computed as normal by a level code as $p = p_{-H} + g\rho(D - H)/2$. Without a bottom boundary layer, this would also be the depth-averaged pressure gradient within the box. However, because the actual thickness of this box is $(D - H - h)$, modifications are needed. These are straightforward. We have

$$\begin{aligned} \int_{-D+h}^{-H} \nabla p \, dz &= \int_{-D+h}^{-H} \nabla \left(p_{-H} - g \int_{-H}^z \rho \, dz' \right) dz \\ &= (D - H - h) \nabla p_{-H} \\ &\quad + \frac{1}{2} (D - H - h)^2 \nabla \rho. \end{aligned} \quad (3.3)$$

Thus

$$\overline{\nabla p} = \nabla p_{-H} + \frac{1}{2} (D - H - h) \nabla \rho. \quad (3.4)$$

In the second term, $(D - H)$ is already accounted for by the usual level code. So the extra term required is merely $-gh \nabla \rho/2$. Here h is a weighted contribution from the four surrounding tracer points, a contribution occurring only if the relevant point lies just above the bottom layer. Thus, in Fig. 3, there is no contribution from point C in the pressure gradient term computed at B.

The barotropic mode is computed for this free surface model as in Killworth et al. (1991) or Webb (1996), although a similar treatment can be made for rigid-lid models. A depth integration of terms contributing to changes of horizontal momentum is made [neglecting Coriolis terms, which are stepped explicitly, as in Killworth et al. (1991), although frictional terms are now included in the depth integration rather than being stepped explicitly; cf. Webb (1996)]. This involves integration of (2.1), (2.2), although varying gridbox depths means that forms similar to (2.16), (2.17) are actually used. As noted above, this integration is over a depth that depends on h . These forcing terms are passed to the time-splitting integrator for the barotropic mode.

Finally, there is no alteration to the manner in which convection is handled. The MOMA code uses the original Cox (1984) formulation of successive pairwise checking for local instability, and this is carried over to the model here. Other convective algorithms would also function normally.

4. A test problem

We now describe the response of the model to an idealized dense outflow problem designed to be a clear, but also appropriate, test of the model dynamics. The domain is a zonally periodic channel, 4° wide and 8° long with one-quarter degree horizontal resolution, centered at 42°N . There are 14 vertical levels, including the bottom layer, with vertical spacing increasing from 30 m at the uppermost level to 740 m at the deepest. The bottom topography varies in the meridional direction only, increasing northward from the middle of the domain by one vertical level at each horizontal grid point. This represents a reduction in depth from 4 km in the south of the domain to 580 m at the northern boundary. The only active tracer is potential temperature, which is initially set to a uniform value of 20°C , so giving unstratified fluid.

For our basic run, surface fluxes of momentum are set to zero and the surface temperature is relaxed toward its initial value of 20°C using a Haney relaxation timescale of 50 days. The principal forcing is due to a localized inflow of dense water at the northern boundary. This inflow is provided by appending a cool basin to the north, which acts as a reservoir of dense fluid. We are not concerned with the dynamics within this cool basin, only with the dense inflow it provides. We note simply that the cool basin has the same zonal extent as the model domain but is closed at either end with a meridional extent of 2° , that the initial temperature in the basin is 10°C , and that the surface temperature is restored to this same value. The two basins are connected by a strait that is one tracer grid cell long and four tracer grid cells, or one degree, in width. Apart from the inflow region, the lateral boundary conditions for the model domain are zero flux at the northern and southern boundaries and periodicity at the eastern and western boundaries. Values for numerical coefficients were standard (in $\text{m}^2 \text{s}^{-1}$), viscosity was 10^4 horizontally, 2×10^{-3} vertically, and diffusion was 2×10^3 horizontally, 10^{-4} vertically.

[Figure 4](#) shows the results after two months of integration. In contrast, [Fig. 5](#) shows the results of two months of integration of an equivalent run without the bottom boundary layer parameterization, injecting the cold water in the lowest grid point. A region of cool, dense water can clearly be seen moving down the slope and spreading westward in the bottom boundary layer, as expected from geostrophic adjustment theory. The maximum velocity at the inflow is around 40 cm s^{-1} , with typical velocities reaching around 70 cm s^{-1} in the dense slope current; the incoming volume flux is $3.6 \times 10^6 \text{ m}^3 \text{ s}^{-1}$. A barotropic flow of maximum velocity around 20 cm s^{-1} has developed, which flows primarily from west to east along the slope. Superimposed on this is a weaker cyclonic barotropic circulation near the source region. This is consistent with the horizontal vorticity tendency of the bottom pressure torque term, through the well-known relation $J(\psi, f/D) = J(E, 1/D)$ where $E = \int_{-D}^0 \rho g z dz$ is potential energy measured relative to the surface, and other forcings, including bottom stress, are neglected. Since $D = D(y)$ only and variations of $1/D$ dominate variations of f , this gives simply $\psi_x = E_x/f$ to leading order. Now E has the same sign as temperature, so E_x is negative west of the inflow and positive east, yielding a cyclonic circulation as observed.

Over the flat bottom in the southern half of the domain there is only relatively weak flow so that for much of the flat region the height of the bottom boundary layer takes its minimum allowed value, which in our simulations is set to 1 m. Stronger flow over the slope gives rise to a deeper bottom layer, with a maximum depth of almost 100 m near the bottom of the slope. Where the layer depth is largest, it is limited mostly by stratification; the rotational depth limit $C_{\eta} u_* / f$ is roughly 180 m at this point, while the stratification limited value $C_{\eta} u_* / N$ is around 140 m. The slope current does not have a very sharply defined nose but, if we arbitrarily choose the 19° contour to define a length scale for the distance travelled by the dense current, we find that after one month the position of this contour has moved about 825 km westward (to obtain this figure we have run the model again using a domain twice as long, to avoid self-interaction of the plume). This gives an average speed of 27.5 cm s^{-1} . The geostrophic slope current velocity scale $g'D_y/f$ (cf. [Nof 1983](#)), by comparison, is about 30 cm s^{-1} , taking a temperature contrast of 1°C and a mean slope of 1.8×10^{-2} , in good agreement with the observed value.

In fact, comparison with plume theory can be made more quantitative. If a turbulent plume descends with speed U down a slope, oriented at an angle θ to the east–west direction, then the two predominant balances become

$$g'D_y \sin\theta = \frac{C_D U^2}{h}; \quad g'D_y \cos\theta = fU$$

so that the angle of fall is given by $\tan\theta = C_D U/fh$. Using values from [Fig. 4](#) for U , h we obtain an angle of fall of about 15° after length scalings are taken into account; $\tan^{-1}(C_D U/fh) = 15^\circ$ also. Thus the approach is generating values similar to those in plume models.

In contrast the run without a bottom layer parameterization has much weaker flow in the layer immediately above the slope. The inflow of dense water produces a strong barotropic circulation, as in the case with a bottom layer, but the dense fluid fails to propagate far either along or down the slope, contrary to expectations and observations of the behavior of true slope currents.

The effects of background flow on plume penetration are complicated by interactions with the strength of the turbulent friction, and other effects. [Figure 6](#) shows the equivalent calculation to [Fig. 4](#), but with a steady westward wind of

maximum strength 0.1 N m^{-2} , varying sinusoidally northward with zero values north and south. This promotes a westward flow, which slightly increases the flow in the boundary layer, leading to a marginally thicker layer, and slightly weakens the topographically forced eastward barotropic flow above.

The basic test run of [Fig. 4](#) has a region of strong entrainment near the inflow with weaker entrainment over the middle of the plume. Detrainment occurs over about half of the plume area, being strongest close to the region of maximum layer height where the slope current meets the flat bottom of the domain. The small temperature perturbations outside of the bottom layer provide evidence that detrainment is weak. Confirmation of the relatively small effect of entrainment and detrainment on the dynamical balance in the bottom layer has been obtained by examination of terms in the model equations. The principal dynamical balance for the baroclinic velocities is between the pressure term, including the terms due to bottom slope, and the Coriolis and bottom drag terms. [Figure 7](#) shows the variation of these three terms in the equation for the northward baroclinic velocity in the bottom layer for a north–south section halfway along the domain.

5. Discussion

We have demonstrated that a turbulent bottom boundary layer can be added to a vertical coordinate model with step topography in a consistent manner and have provided a code written within the framework of an existing popular model code. Appendix A shows that the code conserves energy (and of course conserves tracers, etc., as in the original codes). The model has been designed so that changing entrainment depth parameterizations would be a straightforward and rapid exercise.

The strength of our model is that the fluxes in and out of the bottom layer are calculated on the basis of physically sensible parameterizations of an equilibrium depth for the layer. Considering the difficulty in obtaining observations of the benthic boundary layer it is clearly desirable to minimize the number of free parameters in any model parameterization of the layer. However, in models with otherwise uniform spatial grids, including most common OGCMs, the spatial and temporal variation of layer depth gives rise to significant increases in storage requirements or alternatively—as in our formulation—cpu requirements. It is worth noting, therefore, that it is the inclusion of downslope pressure forces that is most important in allowing the model to simulate dense slope flows. The extra computational requirements of our model, on the other hand, are dominated by the calculation of the height of the layer. Experience with models at least as advanced as ours might provide enough knowledge of the behavior of the bottom layer to parameterize the variation of bottom layer depth both with more computational efficiency and more confidence, without sacrificing the essential extra physics.

Finally, although the tests described here are in idealized circumstances, we can note that K. Stratford (1996, personal communication) has incorporated the code into an eddy-permitting model of the Mediterranean; the code runs without any difficulties.

Acknowledgments

This work was performed under NERC Grant GR3/08578. Discussions with colleagues, especially George Nurser, are gratefully acknowledged. We thank Kevin Stratford for locating an error in the code.

REFERENCES

- Armi, L., and R. C. Millard, 1976: The bottom boundary layer of the deep ocean. *J. Geophys. Res.*, **81**, 4983–4990.
- Baringer, M. O., and J. F. Price, 1997a: Mixing and spreading of the Mediterranean outflow. *J. Phys. Oceanogr.*, **27**, 1654–1677. [Find this article online](#)
- , and —, 1997b: Momentum and energy balance of the Mediterranean outflow. *J. Phys. Oceanogr.*, **27**, 1678–1692. [Find this article online](#)
- Beckmann, A., and R. Döscher, 1997: A method for improved representation of dense water spreading over topography in geopotential-coordinate models. *J. Phys. Oceanogr.*, **27**, 581–591. [Find this article online](#)
- Cox, M. D., 1984: A primitive equation, 3-dimensional model of the ocean. GFDL Ocean Group Tech. Rep. 1, GFDL, Princeton University, Princeton, NJ, 143 pp.
- Deardorff, J. W., 1972: Parameterization of the planetary boundary layer for use in general circulation models. *Mon. Wea. Rev.*, **100**, 93–106. [Find this article online](#)
- Dietrich, D. E., M. G. Marietta, and P. J. Roache, 1987: An ocean modelling system with turbulent boundary layers and topography: Numerical description. *Int. J. Num. Meth. Fluids*, **7**, 833–855.
- Dynamo Group, 1997: DYNAMO: Dynamics of North Atlantic models: Simulation and assimilation with high resolution models. MAS2-CT93-0060, 363 pp.
- Emms, P. W., 1998a: Streamtube models of gravity currents in the ocean. *Deep-Sea Res.*, **44**, 1575–1610.

— 1998b: A streamtube model of a rotating turbidity current *J. Mar. Res.*, **56**, 41–74..

Fohrmann, H., J. O. Backhaus, F. Blaume, and J. Rumohr, 1998: Sediments in bottom arrested gravity plumes: Numerical case studies. *J. Phys. Oceanogr.*, **28**, 2250–2274.. [Find this article online](#)

Gnanadesikan, A., 1999: Representing the bottom boundary layer in the GFDL ocean model: Model framework, dynamical impacts, and parameter sensitivity. *J. Phys. Oceanogr.*, in press..

Haney, R. L., 1991: On the pressure gradient force over steep topography in sigma coordinate ocean models. *J. Phys. Oceanogr.*, **21**, 610–619.. [Find this article online](#)

Hughes, C. W., 1995: A warning about topography in the Cox code. *Ocean Modeling* (unpublished manuscript) **106**..

Johnson, G. C., T. B. Sanford, and M. O. Baringer, 1994: Stress on the Mediterranean outflow plume: Part I. Velocity and water property measurements. *J. Phys. Oceanogr.*, **24**, 2072–2083.. [Find this article online](#)

Jungclaus, J. H., and J. O. Backhaus, 1994: Application of a transient reduced gravity plume model to the Denmark Strait overflow. *J. Geophys. Res.*, **99**, 12 375–12 396..

— — and H. Fohrmann, 1995: Outflow of dense water from the Storfjord in Svalbard: A numerical model study. *J. Geophys. Res.*, **100**, 24 719–24 728..

Killworth, P. D., 1977: Mixing on the Weddell Sea continental slope. *Deep-Sea Res.*, **24**, 427–448..

— — D. Staniforth, D. J. Webb, and S. Paterson, 1991: The development of a free surface Bryan–Cox–Semtner model. *J. Phys. Oceanogr.*, **21**, 1333–1348.. [Find this article online](#)

Mellor, G. L., and T. Yamada, 1974: A hierarchy of turbulence closure models for planetary boundary layers. *J. Atmos. Sci.*, **31**, 1791–1806.. [Find this article online](#)

Nof, D., 1983: The translation of isolated eddies on a sloping bottom. *Deep-Sea Res.*, **30**, 171–192..

Nurser, A. J. G., 1996: A review of models and observations of the oceanic mixed layer. Southampton Oceanography Centre Internal Document No. 14, 247 pp..

Pratt, L. J., and P. A. Lundberg, 1991: Hydraulics of rotating strait and sill flow. *Annu. Rev. Fluid Mech.*, **23**, 81–106..

Price, J. F., and M. O. Baringer, 1994: Outflows and deep water production by marginal seas. *Progress in Oceanography*, Vol. 33, Pergamon, 161–200..

Rosby, C. G., and R. B. Montgomery, 1935: The layer of frictional influence in wind and ocean currents. *Pap. Phys. Oceanogr. Meteor.*, **3**, 1–101..

Smith, P. C., 1975: A streamtube model for bottom boundary currents in the ocean. *Deep-Sea Res.*, **22**, 853–873..

Webb, D. J., 1996: An ocean model code for array processor computers. *Comput. Geosci.*, **22**, 569–578..

Zilitinkevich, S., and D. V. Mironov, 1996: A multi-limit formulation for the equilibrium depth of a stably stratified boundary layer. *Bound.-Layer Meteor.*, **81**, 325–351..

APPENDIX A

6. Energetics

It is important to ensure that the total energy is conserved by both the continuous and finite-difference versions of the system, apart from frictional, diabatic, and turbulent changes. We consider first the continuous, and then the discrete, forms.

a. Continuous equations

In the continuous form, we have

$$\int_A \left[\frac{\partial}{\partial t} \int_{-D}^0 \frac{1}{2} (u^2 + v^2) dz \right] + \frac{\partial}{\partial t} \int_{-D+h}^0 \frac{1}{2} (u^2 + v^2) dz, \quad (\text{A.1})$$

where A is the horizontal ocean area, and dA denotes an element of it. The integral has been split into boundary layer and interior components. We first examine the boundary layer term. Using (2.15) to (2.17) gives, after some algebra,

$$\begin{aligned} \frac{\partial}{\partial t} \int_{-D}^{-D+h} \frac{1}{2} u^2 dz &= -\nabla \cdot \left(\mathbf{u}_m h \frac{u_m^2}{2} \right) + f h u_m v_m \\ &\quad - \frac{h}{\rho_0} u_m \overline{p_{mx}} \\ \frac{\partial}{\partial t} \int_{-D}^{-D+h} \frac{1}{2} v^2 dz &= -\nabla \cdot \left(\mathbf{u}_m h \frac{v_m^2}{2} \right) - f h u_m v_m \\ &\quad - \frac{h}{\rho_0} v_m \overline{p_{my}} \end{aligned}$$

so that

$$\frac{1}{\rho_0} \frac{\partial}{\partial t} \text{KE}|_{\text{bottom}} = - \int_A dA \frac{1}{\rho_0} \{ u_m h \overline{p_{mx}} + v_m h \overline{p_{my}} \}$$

since other terms either cancel or are divergences. Using the definition of $\overline{p_{mx}}$, etc., this simplifies to

$$\frac{1}{\rho_0} \frac{\partial}{\partial t} \text{KE}|_{\text{bottom}} = - \frac{1}{\rho_0} \int_A dA \left\{ -p_i \nabla \cdot (h \mathbf{u}_m) + g h \rho_m \mathbf{u}_m \cdot \nabla (h - D) + \frac{g h^2}{2} \mathbf{u}_m \cdot \nabla \rho_m \right\}. \quad (\text{A.2})$$

(Click the equation graphic to enlarge/reduce size)

Here divergences and gradients are two-dimensional.

We also have

$$\begin{aligned} \frac{1}{\rho_0} \frac{\partial}{\partial t} \text{KE}|_{\text{interior}} &= \int_A dA \left\{ -\frac{h_t}{2} (u_i^2 + v_i^2) - \int_{-D+h}^0 \nabla \cdot \left(\mathbf{u} \frac{1}{2} (u^2 + v^2) \right) dz - \int_{-D+h}^0 \frac{1}{\rho_0} (u p_x + v p_y) dz \right\} \\ &= \int_A dA \left\{ \frac{1}{2} (u_i^2 + v_i^2) \nabla \cdot (\mathbf{u}_m h) + w_i \frac{1}{2} (u_i^2 + v_i^2) - \mathbf{u}_i \frac{1}{2} (u_i^2 + v_i^2) \cdot \nabla (-D + h) \right. \\ &\quad \left. - \frac{1}{\rho_0} \int_{-D+h}^0 [\nabla \cdot (\mathbf{u} p) + w \rho g] dz \right\} \end{aligned}$$

(Click the equation graphic to enlarge/reduce size)

after considerable algebra. The second and third terms cancel from the definition of w_i , the first term can be simplified, and the horizontal part of the three-dimensional divergence vanishes, giving

$$\frac{1}{\rho_0} \frac{\partial}{\partial t} \text{KE}|_{\text{interior}} = \int_A dA \left\{ \frac{h_t p_i}{\rho_0} - \frac{1}{\rho_0} \int_{-D+h}^0 w \rho g dz \right\} \quad (\text{A.3})$$

so that

$$\frac{\partial}{\partial t} \text{KE} = \int_A dA \left\{ -gh\rho_m \mathbf{u}_m \cdot \nabla(h - D) - \frac{gh^2}{2} \mathbf{u}_m \cdot \nabla \rho_m - \int_{-D+h}^0 w\rho g dz \right\}. \quad (\text{A.4})$$

The contribution from potential energy is simpler:

$$\begin{aligned} \frac{\partial}{\partial t} \text{PE} &= \int_A dA \int_{-D}^0 \rho g z dz \\ &= \int_A dA \left\{ \frac{\partial}{\partial t} \int_{-D}^{-D+h} \rho g z dz + \frac{\partial}{\partial t} \int_{-D+h}^0 \rho g z dz \right\} \\ &= \int_A dA \left\{ h_t \rho_m g (-D + h) + \rho_{mt} g \int_{-D}^{-D+h} z dz - h_t \rho_i g (-D + h) + \frac{\partial}{\partial t} \int_{-D+h}^0 \rho_i g z dz \right\}. \end{aligned} \quad (\text{A.5})$$

Assuming linear equations of state and use of (2.5), (2.6), (2.18), and (2.19), manipulation leads to

$$\frac{\partial}{\partial t} \text{PE} = \int_A dA \left\{ g\rho_m h_t (-D + h) + \frac{g\rho_{mt}}{2} h (h - 2D) + \int_{-D+h}^0 w\rho g dz \right\}. \quad (\text{A.6})$$

Adding (A.4) and (A.6), and use of the representations for time derivatives in terms of horizontal gradients, gives

$$\begin{aligned} \frac{\partial}{\partial t} (\text{KE} + \text{PE}) &= \int_A dA \left\{ -gh\rho_m \mathbf{u}_m \cdot \nabla(h - D) - \frac{gh^2}{2} \mathbf{u}_m \cdot \nabla \rho_m - g\rho_m (-D + h) \nabla \cdot (h\mathbf{u}_m) - \frac{gh}{2} (h - 2D) \mathbf{u}_m \cdot \nabla \rho_m \right\} \\ &= -g \int_A dA \{ \rho_m (h - D) \nabla \cdot (h\mathbf{u}_m) + \rho_m h \mathbf{u}_m \cdot \nabla (h - D) + h(h - D) \mathbf{u}_m \cdot \nabla \rho_m \} \\ &= -g \int_A dA \nabla \cdot \{ \rho_m h \mathbf{u}_m (h - D) \} = 0 \end{aligned} \quad (\text{A.7})$$

(Click the equation graphic to enlarge/reduce size)

so that total energy is conserved.

b. Finite-difference form

In the finite-difference version, both the bottom layer and the layer above have variable depth. To account for this we need to add “extra” pressure terms in both layers: in the bottom layer as defined in [section 2](#) and analogously in the layer above. Here we show that the discretization of these extra terms can be chosen such that an averaged form of energy is

conserved spatially in the interior of the fluid. We consider only the advective part of the time step, as energy should not be conserved in the process of turbulent entrainment.

Without a bottom boundary layer sensible choices of discretization lead to exact conservation of energy in time and space by the diffusive and advective terms in the equations, at least in the idealized case of a linear equation of state. With the variable depth bottom layer we can retain a spatial form of energy conservation, but it is not possible to conserve energy exactly in time (using finite-differenced time stepping) in the same way because the energy form now involves products of three temporally varying quantities, that is, the layer height and the square of the velocity rather than quadratic terms in codes without bottom boundary layers. In spite of this we consider the spatial conservation property demonstrated below to be an important attribute of our code. We assume that the bottom is locally flat since the momentum equations are not defined at steps where the velocity is zero, but the cancellation between those terms that are defined at steps is consistent with the cancellation of interior terms, which we demonstrate below for a flat bottom.

Defining

$$\delta_x a \equiv [a(x + \Delta x/2) - a(x - \Delta x/2)]/\Delta x \quad (\text{A.8})$$

in addition to (3.2), the following relations can easily be verified:

$$\overline{a\delta_x b^x} + b\delta_x a = \delta_x(\overline{ab^x}) \quad (\text{A.9})$$

$$\overline{a^x\delta_x b} + \overline{b^x}\delta_x a = \delta_x(\overline{ab}) \quad (\text{A.10})$$

$$\overline{ab^x} - \overline{a^x b^x} = \delta_x(b\delta_x a). \quad (\text{A.11})$$

We also use the fact that in regions where the grid spacing remains constant—that is, away from the bottom layer—quadratic quantities are conserved in the same way as in the normal code; consider a quantity q and let $\mathbf{F} = (F^x, F^y, F^z)$ be the advective flux between q cells. Away from the bottom layer the rate of change of the sum of q^2 values can be discretized as

$$2 \sum q \delta_t q \Delta x \Delta y \Delta z, \quad (\text{A.12})$$

where the sum is taken over all interior q points. We are concerned here with the advective contribution to this sum, which is

$$\begin{aligned} A &= 2 \sum q [\delta_x(\overline{q^x F^x})\Delta x + \delta_y(\overline{q^y F^y})\Delta y + \delta_z(\overline{q^z F^z})\Delta z] \\ &= \sum [q^2(\delta_x F^x \Delta x + \delta_y F^y \Delta y + \delta_z F^z \Delta z) \\ &\quad + q_{ijk}(q_{i+1jk} F_{ijk}^x - q_{i-1jk} F_{i-1jk}^x + q_{ij+1k} F_{ijk}^y \\ &\quad - q_{ij-1k} F_{ij-1k}^y + q_{ijk+1} F_{ijk}^z \\ &\quad - q_{ijk-1} F_{ijk-1}^z)], \end{aligned} \quad (\text{A.13})$$

where $q_{ijk} = q(i\Delta x, j\Delta y, k\Delta z)$, $F_{ijk}^x = F^x[(i + 0.5)\Delta x, j\Delta y, k\Delta z]$, and F^y, F^z are defined analogously between q points. The vertical velocity is defined such that the first term in brackets (proportional to $\nabla \cdot \mathbf{F}$) is zero, while the remaining terms cancel in pairs between adjacent terms in the sum. Hence $A = 0$ unless there are nonzero fluxes across boundaries.

The kinetic energy is defined by

$$\text{KE} = \rho_0 \sum \frac{1}{2} (u^2 + v^2) \Delta x \Delta y \Delta z_u, \quad (\text{A.14})$$

where the sum is taken over all interior velocity points and the subscript u again denotes values at velocity points. The area element $\Delta x \Delta y$, which is constant, will henceforth be suppressed. Hence

By virtue of (A.13), the only advective contribution to the first term in this sum comes from $z = -D + h$ where the vertical flux is taken to be zero before entrainment. Hence the advective contribution to (A.15) consists of the unbalanced contributions to the energy flux divergence on either side of $z = -D + h$. The vertical flux occurs with opposite sign above and below $z = -D + h$, so the resulting contribution can be rearranged to give

$$\sum w(\bar{u}^z \delta_z u + \bar{v}^z \delta_z v) \Delta z_w,$$

where Δz_w is the vertical separation of horizontal velocity points (i.e., the vertical spacing centered at w points). The sum is taken over horizontal points evaluated at the vertical level $z = -D + h$. Combining this with the second term in (A.15), we find the remaining interior contribution to (A.15) to be the following sum over the same set of points:

$$R = - \sum \left(w(\bar{u}^z \delta_z u + \bar{v}^z \delta_z v) - \frac{1}{2} \delta_r h_u \delta_z (u^2 + v^2) \right) \Delta z_w. \quad (\text{A.16})$$

At tracer points $w = h_p$, whereas at velocity points this holds only in horizontal average, so the advective contribution is approximately zero subject to appropriate definition of the second term in (A.15). Since the precise discretization of (A.15) is somewhat arbitrary owing to the lack of exact conservation in time, this approximation is not a significant source of error.

Before adding the extra pressure terms, the pressure gradient contribution to KE_t is

$$- \sum \left(u \Delta z_u \overline{\delta_x p^y} + v \Delta z_u \overline{\delta_y p^x} \right) \quad (\text{A.17})$$

$$= \sum \left(\overline{p \left(\delta_x u \Delta z_u^y + \delta_y v \Delta z_u^x \right)} \right) + D_1 \quad (\text{A.18})$$

$$= - \sum \overline{p \delta_z w \Delta z_\rho^x} + D_2 \quad (\text{A.19})$$

$$= \sum \overline{w \delta_z p \Delta z_w^x} + D_3 \quad (\text{A.20})$$

$$= -g \sum \overline{w \bar{\rho}^z \Delta z_w^x} + D_4. \quad (\text{A.21})$$

The D_i are difference terms that do not contribute to the sum in the interior of the ocean.

The extra pressure gradient term in the bottom layer, from (2.14), is discretized as

$$\begin{aligned} & -g \sum \left(\overline{\bar{\rho}_x \delta_x z_\rho^y} u \Delta z_u + \overline{\bar{\rho}_y \delta_y z_\rho^x} v \Delta z_u \right) \\ & = -g \sum \left(\overline{\bar{\rho}^x \delta_x z_\rho u \Delta z_u^y} + \overline{\bar{\rho}^y \delta_y z_\rho v \Delta z_u^x} \right) + D_5. \end{aligned} \quad (\text{A.22})$$

In the layer above the bottom layer, the extra pressure term in the x -momentum equation required numerically (but not analytically since that problem is continuous) is discretized as $-g \bar{z}_\rho^x \bar{\delta}_x \bar{\rho}^y$, where z_ρ is taken relative to the constant height z_ρ at the center of the original grid cell so that $z_\rho = h/2$ where the bottom is flat, or 0 on the lower side of a step where $\Delta z_\rho = \Delta z_0$ (see Fig. A1). Thus we get a contribution to KE_t of

Another case considered by Gnanadesikan is slightly adapted here. It proves to be useful for estimates of erroneous pressure gradients, as we shall see. We consider the case when the interior density is $\rho_I(z)$ and the boundary layer density is $\rho_m = \rho_I(-D + h/2)$, that is, the density of the interior fluid at the middle of the boundary layer. This density is linear in z for simplicity. In the limiting case of no layer thickness, then there is no pressure gradient, as noted in [section 2](#). Otherwise, computing [\(2.14\)](#) gives

$$\overline{\nabla p_m} = -\frac{g}{4}\rho_{Iz}h\nabla h, \quad (\text{B.1})$$

where the vertical gradient of ρ_I is not necessarily related to the buoyancy frequency, since we suggest that functions of depth be removed from the equation of state as in sigma-coordinate models and as recommended by [Gnanadesikan \(1999\)](#). This gradient varies with the square of h , represents a true pressure gradient, and vanishes when h vanishes.

There are several ways one can construct the numerical equivalent, in increasing order of “distance” from the analytical equivalent. The simplest case is to retain the analytic structure in the vertical but to replace horizontal gradients by finite differences. This, as in [Gnanadesikan \(1999\)](#), leads to the identical result. The next case replaces the vertical structure with finite differences as well, with the density of each box (both internal and bottom layer) given as the value of the linear stratification in that box. Assume for the moment that there is an increase in depth of one depth box in the x direction. At the first x point, there is a vertical collection of levels (with no flow and no horizontal pressure gradient) above the bottom internal grid box, which has thickness Δz_1 and density ρ_I . The density in the bottom boundary layer beneath is ρ_{MA} , and its height is h_A . At the next x grid point, there is one lower internal box, of density ρ_2 , beneath which is a bottom boundary layer of density ρ_{MB} . These densities are all given by the formula $\rho = \rho_I + \alpha z$, where z is measured from the center of the ρ_I box (where horizontal pressure gradients are assumed zero), and α is the vertical density gradient, subject to the above comments. Some algebra then gives

$$\begin{aligned} \overline{\nabla p_m} = \frac{g\alpha}{\Delta x} \left\{ \frac{1}{8}(\Delta z_2^2 - \Delta z_1^2) + \frac{1}{2}(\Delta z_1 h_A - \Delta z_2 h_B) \right. \\ \left. + \frac{3}{8}(h_B^2 - h_A^2) \right\}. \end{aligned} \quad (\text{B.2})$$

The three terms in this expression play differing roles. The first vanishes when the vertical grid spacing is uniform. Otherwise, this term represents an error, of order $g\rho_{Iz}\Delta z\nabla D$. The second and third terms can be combined to give a gradient of order $^{-1/2}g\rho_{Iz}\{\Delta z - [\text{xe}3]_3^4(h_A + h_B)\}(h_B - h_A)/\Delta x$, ignoring differences in vertical spacing. This expression is similar to the analytic solution, with two changes. The numerical coefficient has altered, and h has been replaced by a depth less than Δz . In some sense, then, the finite vertical spacing has expanded the thickness h to something close to the grid spacing itself. If the step occupies more than one grid point [recall the [Hughes \(1995\)](#) arguments against such a choice], then additional terms are involved.

The final version of the problem retains a similar structure to that just discussed, save that the boundary layer has the same density as the box just above it. We again assume that the step involves only one grid box. Then after some algebra

$$\overline{p_{mx}} = \frac{g}{4\Delta x}(\Delta z_1 + \Delta z_2 - h_A - h_B)(\rho_2 - \rho_1). \quad (\text{B.3})$$

[Precisely the same is found using [\(2.14a\)](#) instead.] Now

$$-(\rho_2 - \rho_1) = -\frac{\rho_{Iz}}{2}(\Delta z_1 + \Delta z_2)$$

(with the same comment about vertical gradient as made above) so, substituting,

$$\overline{p_{mx}} = -\frac{g\rho_{Iz}}{8}(\Delta z_1 + \Delta z_2 - h_A - h_B)\frac{(\Delta z_1 + \Delta z_2)}{\Delta x},$$

SO

$$|\overline{p_{mx}}| \leq -\frac{g\rho_{Iz}}{2}\frac{\Delta z^2}{\Delta x} = -\frac{g\rho_{Iz}}{2}\Delta z|\nabla D| \quad (\text{B.4})$$

if grid spacings are equal, for simplicity. This has essentially replaced h and ∇h in (B.1), respectively, by Δz and ∇D in (B.4). This occurs because the thickness of the bottom boundary layer has now effectively been expanded over the entire grid box.

If the step consists of more than one grid point, it is straightforward to show that the second term is small if the density is roughly linear with depth. The first term is now modified and gives approximately

$$|\overline{p_{mx}}| \leq -\frac{g\rho_{Iz}}{2} E \frac{\Delta z}{\Delta x},$$

where E is the height of the step,

$$= -\frac{g\rho_{Iz}}{2} \Delta z |\nabla D|,$$

once again. (This assumes uniformity of the interior density gradient over the N grid points.)

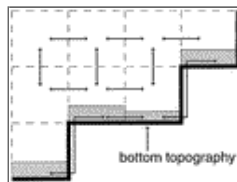
In both versions of this case, the pressure gradients can produce flows that vary from negligible to $O(1 \text{ cm s}^{-1})$, depending on parameters chosen. Whether these flows are serious overestimates of reality will depend on the size of h . If h takes its minimum value (chosen here as a 1 m cutoff), then steep gradients and large interior density gradient can combine to give a large error term. If, however, h is a reasonable fraction of the bottom grid box thickness, then the pressure gradient induced will be approximately correct.

This case has been tested numerically, using the same model domain as in section 4 of this paper (i.e., without the cool basin), with the initial temperature of the bottom layer given by the linear gradient evaluated at the midpoint of the bottom layer, as above. We took $T_{Iz} = 2 \times 10^{-3} \text{ }^\circ\text{C m}^{-1}$ and uniform salinity, similar to Gnanadesikan's (1999) test case, and retained a nonlinear equation of state. With the steep gradient of this configuration (1.8×10^{-2}), flows of up to 5 cm s^{-1} were rapidly generated but equilibrated, remaining essentially unchanged during a two-month integration. A second test using a three gridpoint vertical fall in topography produced similar flows.

We follow Gnanadesikan (1999) by recommending that erroneous pressure gradients be minimized by subtracting the areal average of density from the equation of state at each level. The density of the bottom boundary layer has anyway to be interpolated between the values it would take were the layer to have that temperature and salinity at the standard depth layers immediately above and below the location of the layer.

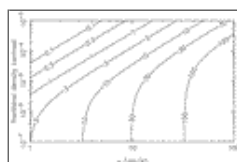
It is not obvious how gradient errors can be reduced below amounts of order $g\rho_{Iz}\Delta z\nabla D$ for general problems. No matter how pressure gradients are evaluated, we believe that errors of this size will always occur due to the coarse finite-difference approaches necessary to fit with the remainder of the code. Other approaches (embedding of a well-resolved bottom boundary layer at the base of the stack of grid boxes) may well be needed but are beyond the scope of this paper.

Figures



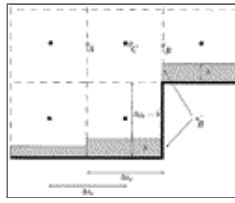
Click on thumbnail for full-sized image.

Fig. 1. Schematic of the bottom boundary layer concept. The thin arrows show the direction and destination of lateral fluxes.



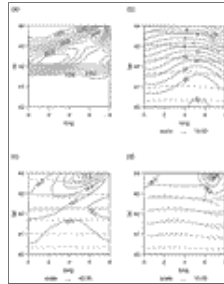
Click on thumbnail for full-sized image.

Fig. 2. Contours of boundary layer depth h (in m) as the bottom boundary layer speed u (cm s^{-1}) and density contrast $\Delta\rho/\rho_0$ vary, at 30°N . The diagram shows a smooth transition from density-dominated thicknesses (upper half) to rotationally dominated thicknesses (lower half).



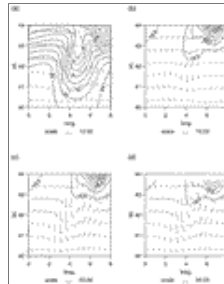
Click on thumbnail for full-sized image.

Fig. 3. Schematic of the grid arrangement for the B-grid model.



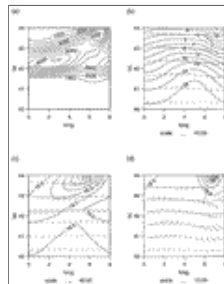
Click on thumbnail for full-sized image.

Fig. 4. Model results after a two-month integration. Shown are (a) depth of bottom boundary layer (cm), (contour interval: 10 m); (b) free surface elevation (contours, cm), contour interval: 4 cm, and barotropic velocity (vectors, every other grid point); (c) bottom boundary layer temperature (contours, °C), contour interval: 0.5°C, and velocity vectors, every other grid point (cm s^{-1}); (d) temperature (contours, °C), contour interval: 0.5°C, and velocity vectors, every other grid point (cm s^{-1}) at 482-m depth.



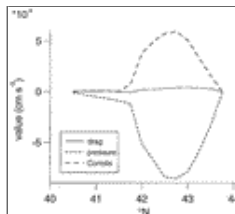
Click on thumbnail for full-sized image.

Fig. 5. Model results after a two-month integration for the problem without a bottom boundary layer. Shown are (a) free surface elevation (contours, cm), contour interval: 4 cm, and barotropic velocity (vectors, every other grid point); (b) temperature (contours, °C), contour interval: 0.5°C, and velocity vectors, every other grid point (cm s^{-1}) at the lowest model level; (c) temperature (contours, °C), contour interval 0.5°C, and velocity vectors at 482 m; (d) as (c), but at next lower depth level.



Click on thumbnail for full-sized image.

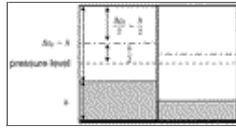
Fig. 6. As for Fig. 4 but with a steady westward wind stress of amplitude 0.1 N m^{-2} varying sinusoidally from zero at north to zero at south, with a maximum at midlatitude.



Click on thumbnail for full-sized image.

Fig. 7. Bottom-layer term balance in the northward momentum equation for the flow in Fig. 4, at midlongitude in the

diagram. All terms are taken to be on the rhs of (2.17) and are divided by depth h . Thus the terms are drag = $-C_D |\mathbf{u}_m| \mathbf{u}_m$,
 pressure = $-\overline{p}_{my}/\rho_0$, Coriolis = $-f\mathbf{u}_m$.



Click on thumbnail for full-sized image.

Fig. A1. The difference in height between pressure levels and the density levels used for energetic calculations.

¹ Models based on other coordinate systems have other problems (Dynamo Group 1997). Sigma-coordinate models have similar, but weaker, behavior—water is still being projected above lighter water, but because of the terrain-following coordinates the effect is less. Isopycnic coordinate models have too little mixing under normal conditions and so move dense water in the densest layer over too great a lateral distance.

² This approach makes it trivial to modify the formula for layer thickness within the code.

³ This gives no formal difficulty at the equator, although Zilitinkevich and Mironov did not test the formula there. We have run wind-forced experiments at the equator with no difficulty.

⁴ This can itself induce difficulties: if the vertical grid spacing is variable, as is customary, then this restriction could cause the layer thickness to vary as the layer descends a slope, for example.

Corresponding author address: Dr. Peter D. Killworth, Southampton Oceanography Centre, Empress Dock, Southampton SO14 3ZH, United Kingdom.

E-mail: P.Killworth@soc.soton.ac.uk

top ▲



© 2008 American Meteorological Society [Privacy Policy and Disclaimer](#)
 Headquarters: 45 Beacon Street Boston, MA 02108-3693
 DC Office: 1120 G Street, NW, Suite 800 Washington DC, 20005-3826
amsinfo@ametsoc.org Phone: 617-227-2425 Fax: 617-742-8718
[Allen Press, Inc.](#) assists in the online publication of *AMS* journals.